Monthly Notices of the ROYAL ASTRONOMICAL SOCIETY

MNRAS **475,** 248–256 (2018) doi:10.1093/mnras/stx3183
Advance Access publication 2017 December 8

VALES – IV. Exploring the transition of star formation efficiencies between normal and starburst galaxies using APEX/SEPIA Band-5 and ALMA at low redshift

C. Cheng,[1,2★] E. Ibar,[1★] T. M. Hughes,[1,2,3,4★] V. Villanueva,[1] R. Leiton,[1] G. Orellana,[1] A. Muñoz Arancibia,[1] N. Lu,[2] C. K. Xu,[2] C. N. A. Willmer,[5] J. Huang,[2] T. Cao,[2] C. Yang,[6,7,8] Y. Q. Xue[3,4] and K. Torstensson[6]

[1]*Instituto de Física y Astronomía, Universidad de Valparaíso, Avda. Gran Bretaña 1111 Valparaíso, Chile*
[2]*Chinese Academy of Sciences South America Center for Astronomy, China-Chile Joint Center for Astronomy, National Astronomical Observatories, Chinese Academy of Sciences, Beijing 100012, China*
[3]*CAS Key Laboratory for Research in Galaxies and Cosmology, Department of Astronomy, University of Science and Technology of China, Hefei 230026, China*
[4]*School of Astronomy and Space Science, University of Science and Technology of China, Hefei 230026, China*
[5]*Steward Observatory, University of Arizona, 933 N. Cherry Avenue, Tucson, AZ 85721, USA*
[6]*European Southern Observatory, Alonso de Cordova 3107, Casilla 19001, Santiago 19, Chile*
[7]*Purple Mountain Observatory/Key Lab of Radio Astronomy, Chinese Academy of Sciences, Nanjing 210008, China*
[8]*Institute d'Astrophysique Spatiale, CNRS, Univ. Paris-Sud, Université Paris-Saclay, Bât. 121, F-91405 Orsay Cedex, France*

Accepted 2017 December 1. Received 2017 December 1; in original form 2017 August 25

ABSTRACT

In this work, we present new the Swedish-ESO PI receiver for the Atacama Pathfinder Experiment APEX/SEPIA Band-5 observations targeting the CO (J = 2–1) emission line of 24 Herschel-detected galaxies at z = 0.1–0.2. Combining this sample with our recent new Valparaíso ALMA Line Emission Survey (VALES), we investigate the star formation efficiencies [SFEs = star formation rate (SFR)/$M_{\rm H_2}$] of galaxies at low redshift. We find the SFE of our sample bridges the gap between normal star-forming galaxies and Ultra-Luminous Infrared Galaxies (ULIRGs), which are thought to be triggered by different star formation modes. Considering the SFE′ as the SFR and the $L'_{\rm CO}$ ratio, our data show a continuous and smooth increment as a function of infrared luminosity (or star formation rate) with a scatter about 0.5 dex, instead of a steep jump with a bimodal behaviour. This result is due to the use of a sample with a much larger range of sSFR/sSFR$_{\rm ms}$ using LIRGs, with luminosities covering the range between normal and ULIRGs. We conclude that the main parameters controlling the scatter of the SFE in star-forming galaxies are the systematic uncertainty of the $\alpha_{\rm CO}$ conversion factor, the gas fraction, and physical size.

Key words: galaxies: ISM – galaxies: starburst – galaxies: star formation – submillimetre: galaxies.

1 INTRODUCTION

The star formation efficiency (SFE) of a galaxy, defined as the ratio between the star formation rate (SFR) and the amount of gas reservoir, is a crucial parameter to characterize its star formation activity and future evolution. Previous studies have shown that the SFE of normal star-forming galaxies (SFGs) is systematically lower than that of starburst galaxies, suggesting different mechanisms could be triggering the star formation (Daddi et al. 2010; Genzel et al. 2010; Carilli & Walter 2013). This lead to a proposal of a bimodal SFE for the two types of SFGs. The first is associated with the 'main sequence' (Brinchmann et al. 2004) formed by normal SFGs, where the star formation is triggered within disc-like structures, and their specific SFR (sSFR = SFR/M_*) slowly decreases with the increasing stellar mass (Schawinski et al. 2014). The second is associated with starburst galaxies that have typical sSFR above the main sequence, and include local Ultra-Luminous Infrared Galaxies (ULIRGs Solomon et al. 1997; Lonsdale, Farrah & Smith 2006). Nevertheless, it is unclear whether the SFE bimodality is caused by a higher gas-to-star conversion rate or simply by a higher fraction of dense molecular gas capable of initiating star formation. Galaxies with SFR in between the ULIRGs and the normal SFGs,

★ E-mail: chengcheng@bao.ac.cn (CC); eduardo.ibar@uv.cl (EI); thomas.hughes@uv.cl (TMH)

e.g. Luminous Infrared Galaxies (LIRGs, $10^{11} < L_{\rm IR}/{\rm L}_{\odot} < 10^{12}$), are a critical population to understand the SFE bimodality.

In studying the SFE in LIRGs, one obstacle is how to measure the molecular hydrogen mass ($M_{\rm H_2}$). Historically, CO has become the most popular tracer of interstellar cold molecular gas. One common method to translate the CO luminosity into the $M_{\rm H_2}$ is the adoption of a simple conversion factor $\alpha_{\rm CO} = M_{\rm H_2}/L'_{\rm CO}$. However, it is challenging to accurately define the value of $\alpha_{\rm CO}$ (Bolatto, Wolfire & Leroy 2013; Carilli & Walter 2013, and references therein). Empirically, the molecular gas clouds in the Milky Way and nearby galaxies show an $\alpha_{\rm CO}$ of $4.6\,{\rm M}_{\odot}\,({\rm K\,km\,s^{-1}\,pc^2})^{-1}$, which includes the helium correction (e.g. Solomon & Vanden Bout 2005). If the molecular clouds in SFGs have similar properties such as metallicity, dynamical state, and gas density, then the $\alpha_{\rm CO}$ of SFG shall resemble that seen in local molecular clouds (Solomon & Vanden Bout 2005). On the other hand, simulations show that galaxy mergers change the cloud and intercloud properties such as the rising of the velocity dispersion and kinetic temperature, which increases the CO intensity (Narayanan et al. 2011). Thus, the $\alpha_{\rm CO}$ of interacting galaxies should drop by a factor of 2–10 (Narayanan et al. 2012a). Detailed modelling and observational results suggest $\alpha_{\rm CO} = 0.8\,{\rm M}_{\odot}\,({\rm K\,km\,s^{-1}\,pc^2})^{-1}$ (Downes & Solomon 1998) as a consistency value to derive $M_{\rm H_2}$ in ULIRGs.

Papadopoulos et al. (2012a,b) found that the $\alpha_{\rm CO}$ in LIRGs can change significantly. Previous studies show that the value of $\alpha_{\rm CO}$ in LIRGs can be similar to that in ULIRGs (Solomon et al. 1997; Yao et al. 2003), where $\alpha_{\rm CO}$ is lower than the Galactic value (e.g. $\alpha_{\rm CO} = 0.5\,{\rm M}_{\odot}\,({\rm K\,km\,s^{-1}\,pc^2})^{-1}$ in VV 114; $\alpha_{\rm CO} = 1.5\,{\rm M}_{\odot}\,({\rm K\,km\,s^{-1}\,pc^2})^{-1}$ in NGC 6240: Sliwa et al. 2013; Tunnard et al. 2015). However, Papadopoulos et al. (2012a,b) also find that the $\alpha_{\rm CO}$ in (U)LIRGs can have values close to those found in the Galaxy (Costagliola et al. 2013; Sandstrom et al. 2013). The kinetic gas components in LIRGs can mix different star formation activities: gas in LIRGs may show compact (Xu et al. 2014) as well as ring structures (Xu et al. 2015). This strongly indicates that the $\alpha_{\rm CO}$ may not have the same value for all LIRGs.

To explore the changing mechanism of the SFE between the 'main sequence' and the starburst regimes, we observe a sample of LIRGs at $0.1 < z < 0.2$ with the Swedish-ESO PI receiver for the Atacama Pathfinder Experiment (APEX/SEPIA, Billade et al. 2012; Belitsky et al. 2017) targeting the CO ($J = 2$–1) emission line. We assume a cosmological model with $H_0 = 70\,{\rm km\,s^{-1}\,Mpc^{-1}}$, $\Omega_{\rm m} = 0.3$, and $\Omega_{\Lambda} = 0.7$.

2 GALAXY SAMPLES AND DATA

2.1 Sample selection

The *Herschel* Astrophysical Terahertz Large Area Survey (*H*-ATLAS; Eales et al. 2010) covered 600 deg^2 of the extragalactic sky with the PACS and SPIRE cameras in the 100, 160, 250, 350, and 500 μm bands. We selected targets from the equatorial *H*-ATLAS fields covered by the Galaxy And Mass Assembly survey that has a rich multiwavelength broad-band coverage (Driver et al. 2016), including *NUV* and *FUV* bands from the *GALEX* imaging, the optical images and spectroscopy from SDSS or GAMA, near-IR imaging from the VISTA project, and mid-IR imaging from *WISE* and the *Herschel* far-IR photometry.

Making use of the public *H*-ATLAS DR1[1] catalogue (Valiante et al. 2016), we select sources with reliable optical counterpart, spectroscopic redshift at $0.1 < z < 0.2$, and located at the top of the sSFR distribution (M_* from GAMA and SFR from $L_{\rm IR}$). These criteria allow weeding out the most intensely starbursting objects from the sample. Using these targets, we explore their molecular gas content via their CO emission. These observations complement our recent Valparaíso ALMA Line Emission Survey (VALES, Villanueva et al. 2017; Hughes et al. 2017a; 2017b), which is the largest CO-detected galaxy sample at $z \sim 0.15$. Fig. 1 shows the sSFR/sSFR$_{\rm ms}$ of the current CO-detected galaxy sample with different redshift. There are several parametrizations of the main-sequence galaxies (e.g. Speagle et al. 2014; Schreiber et al. 2015). As the follow up work of our VALES project, we adopt the sSFR = sSFR(M_*, z) given by Genzel et al. (2015) as the VALES I paper (Villanueva et al. 2017).

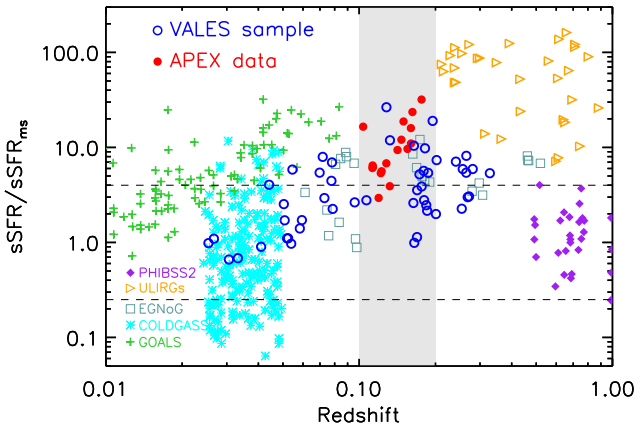

Figure 1. The specific star formation rate (sSFR = SFR/M_*), normalized to that estimated for the 'main sequence' (MS, Elbaz et al. 2011; Whitaker et al. 2012) as a function of redshift for different samples of galaxies detected in CO. We use the parametrization of the MS as $\log[{\rm sSFR(MS},z,M_*)] = -1.12 + 1.14z - 0.19z^2 - (0.3 + 0.13z) \times (\log M_* - 10.5)\,({\rm Gyr^{-1}})$ (Genzel et al. 2015), where the dashed lines represent +/− 0.6 dex offsets from this relation for SFGs. Our VALES data are presented as blue open circles for ALMA and red solid circles for APEX observations. The green crosses are the IRS bright local galaxies (GOALS: Armus et al. 2009); the cyan asterisks are the nearby MS galaxies (COLDGASS: Saintonge et al. 2011); the light blue open squares are $z = 0.05$–0.5 normal galaxies (EGNoG: Bauermeister et al. 2013); the orange open triangles are the ULIRGs at intermediate redshifts (Combes et al. 2011, 2013); the purple diamonds are the MS galaxies at $0.5 < z < 1$ (PHIBSS: Combes et al. 2016). More details about these archive data can be found in the fig. 1 of Genzel et al. (2015). The grey shaded region in this figure shows our target selection within $0.1 < z < 0.2$, which includes the CO ($J = 1$–0) ALMA Band-3 detected galaxies and the CO ($J = 2$–1) APEX/SEPIA Band-5 detected galaxies.

2.2 APEX/SEPIA Band-5 observations

SEPIA Band-5 is a spectrograph that covers the frequency range 159–211 GHz, recently mounted at APEX. The water absorption line at 183 GHz is the main feature of the atmosphere at these frequencies. SEPIA Band-5 is the only instrument that is able to detect CO ($J = 2$–1) at redshifts from 0.1 to 0.2 in the Southern hemisphere. We were awarded 21h of APEX/SEPIA Band-5 observations to target the CO ($J = 2$–1) emission of 24 starburst galaxies (APEX programs 097.F-9724(A); 098.F-9712(B), PI: E. Ibar). Each target's exposure time was about 40min, reaching an rms of about

[1] http://www.h-atlas.org/public-data/download

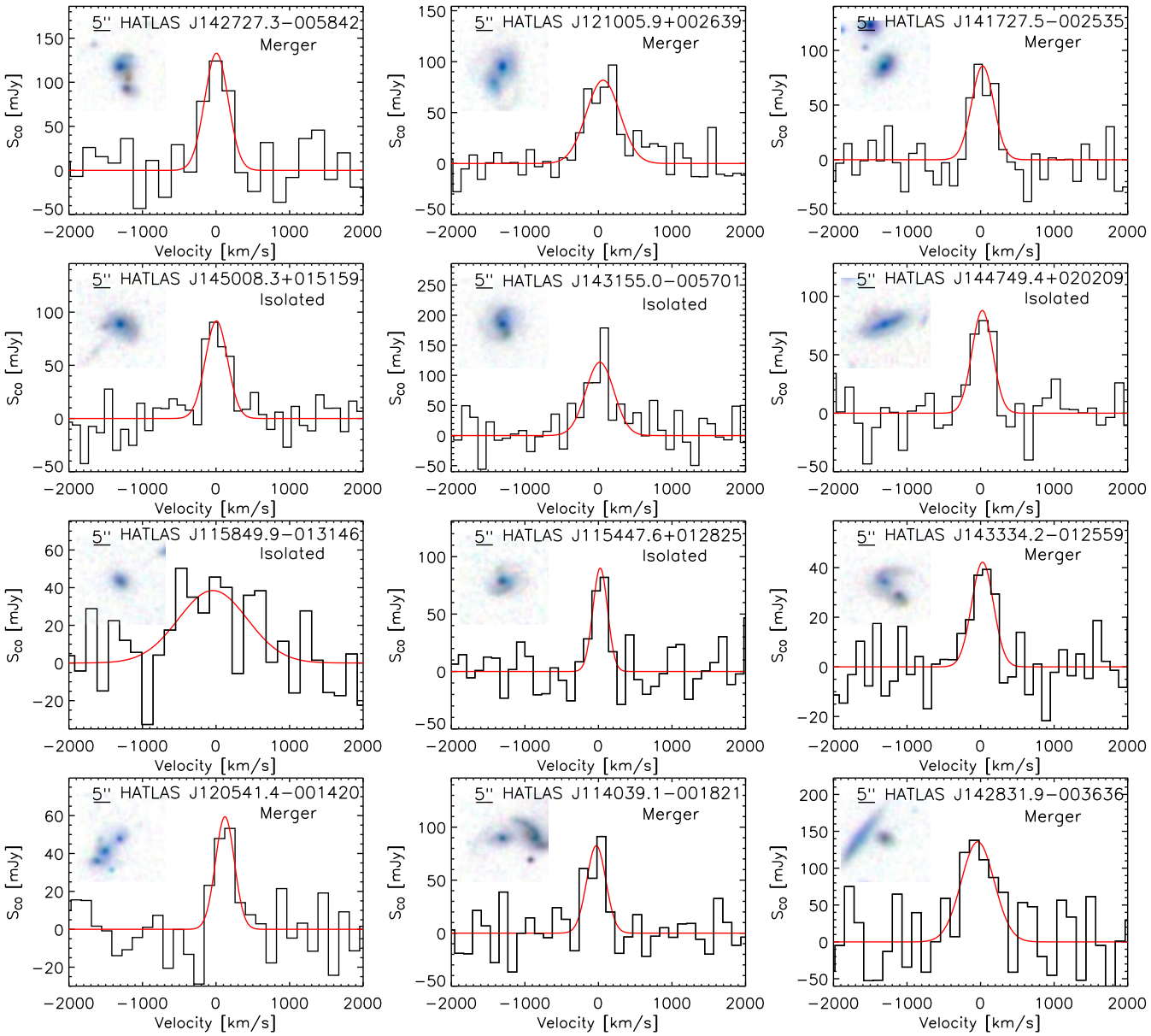

Figure 2. The observed CO ($J = 2$–1) spectra for APEX/SEPIA Band-5 observed galaxies centred on spectroscopic redshifts taken from GAMA. The postage image in the upper left-hand panel of each spectrum comes from the SDSS colour image with a scale of 25 × 25 arcsec^2. The scale bar in the optical image denotes a length of 5 arcsec. The top 12 galaxies have CO detection with 5σ. We fit the CO emission by a single Gaussian profile and show the result as a red line. Typical FWHM is 300 km s^{-1}. HATLAS J115849.9−013146 is an isolated galaxy with fitted FWHM of about 1000 km s^{-1}, much larger than that of other galaxies. This galaxy is isolated and located in a group of three galaxies at $z = 0.147$ within 65 kpc ($\simeq$ 25.3 arcsec). The Petrosian radii of these three galaxies are 2.99, 2.63, and 2.89 arcsec, corresponding to a physical Petrosian diameter about 15 kpc. The first four targets have lower S/N between 3 and 5. We also fit the CO emission by a single Gaussian profile and show the result as a red line. The final eight galaxies have no clear CO emission.

0.5 mK at 111 km s^{-1} channel width. The measured precipitable water vapour during the observations was about 0.8 (in a range between 0.6 and 1.2). The APEX/SEPIA Band-5 data were reduced with CLASS software Version 1.1. For every target, we trimed the edge (about 3 per cent) of the spectrum and subtracted the baseline by using a first-order polynomial. Fig. 2 shows the CO line observations: 16 galaxies have S/N>3 and were fitted by single Gaussian profile (the top 12 spectra in Fig. 2 have S/N>5). 8 galaxies have no CO detection down to 5σ in the APEX spectra. In Fig. 2 we also show the SDSS postage image of each target in the upper-left corner of the CO spectrum.

2.3 Galaxy Sample over $0.1 < z < 0.2$ for this study

We have combined these new SEPIA Band-5 observations to the VALES sample. We select the 16 galaxies with APEX/SEPIA Band-5 detections together with the 17 galaxies previously detected by ALMA and shown by Villanueva et al. (2017) in the same redshift

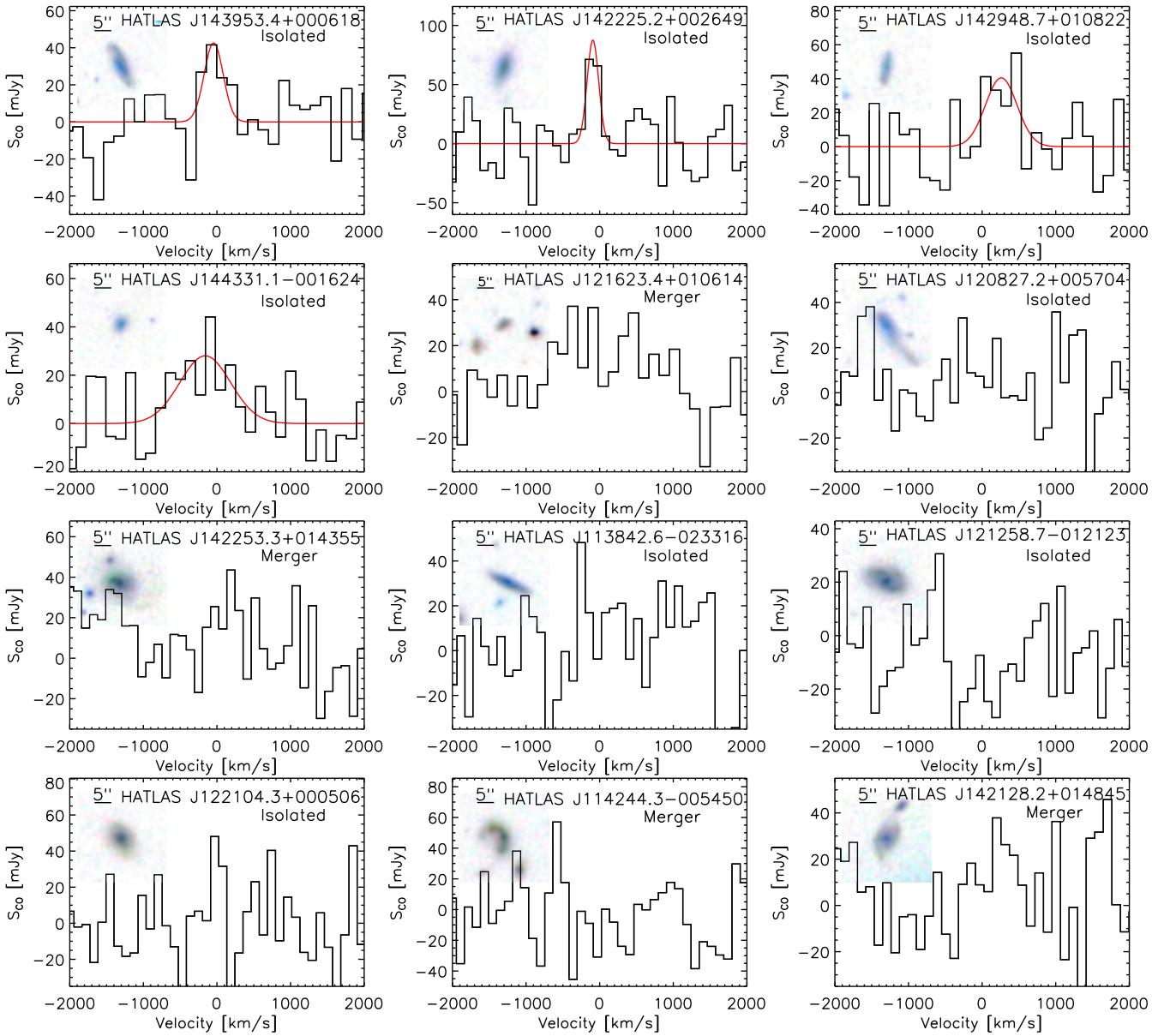

Figure 2 – *continued*

range. These 33 galaxies between $0.1 < z < 0.2$ lie in the grey shaded region of Fig. 1. The cosmological time-scale within this redshift range $\Delta z(0.1 - 0.2)$ is about 1 Gyr, which is about the typical gas depletion time-scale of normal SFGs. Thus the cosmological evolution of the galaxies in this sample can be neglected for normal galaxies, although many starburst cycles could be expected for more active galaxies.

Based on the visual inspection of SDSS images of the 16 APEX galaxies, we identify 7 possibly interacting (mergers) and 9 isolated galaxies. On the other hand, the 17 ALMA CO-detected galaxies include 3 mergers and 14 isolated galaxies. The stellar masses are derived using MAGPHYS (da Cunha, Charlot & Elbaz 2008), whereas the $\mathrm{SFR}(\mathrm{M}_\odot/\mathrm{yr}) = 10^{-10} L_{\mathrm{IR}}/\mathrm{L}_\odot$ (Villanueva et al. 2017) masses are derived using the $L_{\mathrm{IR}}(8\text{–}1000\,\mu\mathrm{m})$ derived from fitting the broad-band far-IR photometry (assuming a Chabrier IMF Chabrier 2003). We follow the same procedure to derive galaxy properties as Villanueva et al. (2017). We list the main properties of the APEX observed targets in Table 1. For the targets with no CO detection, we list the upper limit (5σ) of the CO flux.

3 RESULTS

We define $\mathrm{SFE}' = \mathrm{SFR}/L'_{\mathrm{CO}}$ and present the observed SFE′ versus L_{IR} in Fig. 3. The $L'_{\mathrm{CO}} = L'_{\mathrm{CO}\,(J=1\text{–}0)}$ is defined as (Solomon & Vanden Bout 2005)

$$L'_{\mathrm{CO}\,(J=1\text{–}0)} = 3.25 \times 10^7 S_{\mathrm{CO}} \Delta v\, \nu_{\mathrm{obs}}^{-2} D_{\mathrm{L}}^2 (1+z)^{-3} (\mathrm{K\,km\,s^{-1}\,pc^2}), \quad (1)$$

where $S_{\mathrm{CO}}\Delta v$ is the velocity-integrated flux density in units of $\mathrm{Jy\,km\,s^{-1}}$, ν_{obs} is the observed frequency of the emission line in GHz, D_{L} is the luminosity distance in Mpc, and z is the redshift. We

Table 1. Parameters of the APEX Observed CO (2-1) detected targets.

HATLAS ID	GAMAID	z_{spec}	$\log(M_*/M_\odot)$	$\log(L'_{CO}[Kkm\,s^{-1}pc^2])$	$\log(L_{IR}/L_\odot)$	$\log(M_{dust}/M_\odot)$	CO FWHM km s^{-1}
HATLAS J114039.1−001821	53812	0.1128	10.50 ± 0.03	9.70 ± 0.09	11.29 ± 0.01	8.00 ± 0.06	304 ± 59
HATLAS J115447.6+012825	219701	0.1497	10.57 ± 0.02	9.74 ± 0.12	11.86 ± 0.02	7.99 ± 0.04	233 ± 52
HATLAS J115849.9−013146	185275	0.1468	10.37 ± 0.03	10.13 ± 0.10	11.54 ± 0.03	8.03 ± 0.03	1102 ± 309
HATLAS J120541.4−001420	55305	0.1763	10.20 ± 0.03	9.74 ± 0.16	11.88 ± 0.03	8.44 ± 0.03	301 ± 60
HATLAS J121005.9+002639	85450	0.1280	10.93 ± 0.03	10.04 ± 0.06	11.65 ± 0.03	8.32 ± 0.05	535 ± 81
HATLAS J141727.5−002535	568216	0.1226	10.86 ± 0.11	9.93 ± 0.06	11.51 ± 0.02	8.23 ± 0.04	354 ± 54
HATLAS J142225.2+002649	92214	0.1130	10.53 ± 0.03	9.49 ± 0.15	11.33 ± 0.03	8.07 ± 0.06	<185 ± 66
HATLAS J142727.3−005842	544759	0.1623	10.80 ± 0.03	10.35 ± 0.08	12.14 ± 0.05	8.57 ± 0.02	375 ± 69
HATLAS J142831.9−003636	568985	0.1037	9.80 ± 0.12	10.07 ± 0.09	11.23 ± 0.02	8.24 ± 0.06	526 ± 137
HATLAS J142948.7+010822	228482	0.1601	10.35 ± 0.05	9.95 ± 0.15	11.50 ± 0.01	8.06 ± 0.06	504 ± 167
HATLAS J143155.0−005701	545019	0.1217	11.05 ± 0.02	9.91 ± 0.08	11.62 ± 0.03	8.15 ± 0.05	450 ± 120
HATLAS J143334.2−012559	492771	0.1600	10.37 ± 0.03	9.80 ± 0.10	11.67 ± 0.02	8.05 ± 0.04	347 ± 88
HATLAS J143953.4+000618	79073	0.1321	10.84 ± 0.06	9.49 ± 0.17	11.35 ± 0.01	8.36 ± 0.07	275 ± 112
HATLAS J144331.1−001624	64970	0.1417	10.25 ± 0.07	9.88 ± 0.11	11.34 ± 0.01	7.90 ± 0.04	810 ± 223
HATLAS J144749.4+020209	343741	0.1193	11.05 ± 0.10	9.76 ± 0.09	11.36 ± 0.01	8.09 ± 0.10	329 ± 62
HATLAS J145008.3+015159	252158	0.1134	10.92 ± 0.02	9.79 ± 0.08	11.59 ± 0.02	8.02 ± 0.03	355 ± 60
HATLAS J120827.2+005704	99268	0.1591	11.09 ± 0.02	<7.60	11.73 ± 0.01	8.30 ± 0.03	–
HATLAS J142253.3+014355	319750	0.1104	10.33 ± 0.03	<7.23	11.24 ± 0.05	7.83 ± 0.04	–
HATLAS J113842.6−023316	123041	0.1050	10.73 ± 0.09	<7.28	11.19 ± 0.04	7.85 ± 0.05	–
HATLAS J121258.7−012123	145195	0.1042	10.67 ± 0.02	<7.14	11.18 ± 0.02	7.89 ± 0.04	–
HATLAS J122104.3+000506	71574	0.1071	9.915 ± 0.03	<7.26	11.19 ± 0.04	7.75 ± 0.05	–
HATLAS J114244.3−005450	534898	0.1076	9.940 ± 0.03	<7.35	11.03 ± 0.06	7.79 ± 0.06	–
HATLAS J142128.2+014845	319694	0.1604	10.34 ± 0.04	<7.61	11.21 ± 0.02	8.41 ± 0.11	–
HATLAS J121623.4+010614	24056	0.1552	9.298 ± 0.10	<7.40	10.72 ± 0.03	8.49 ± 0.10	–

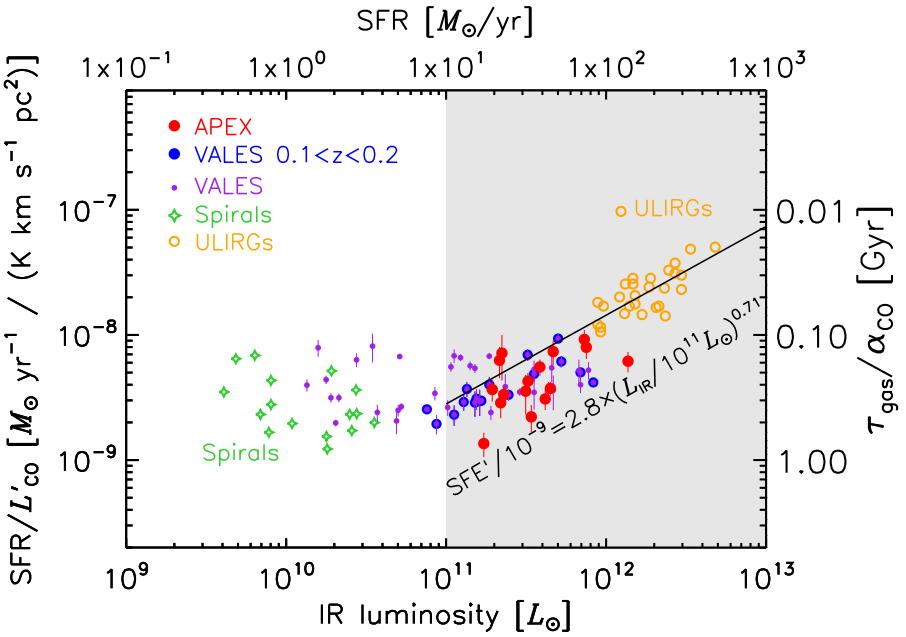

Figure 3. The SFE′(= SFR/L'_{CO}) versus L_{IR} of our CO detected sample (blue and red dots), the VALES sample (purple/blue/red dots), local spirals (green stars; Leroy et al. 2009), and the local ULIRGs (orange circles; Solomon et al. 1997). The top label shows the SFR scale. The L_{IR} is derived from the *Herschel* data fitting as described in Villanueva et al. (2017). The right-hand Y-axis is the gas depletion time-scale normalized by α_{CO}. The SFE′ is nearly constant with 0.5 dex scatter at the IR luminosities between 2×10^9 $L_\odot$ and $\times$ 10^{11} $L_\odot$. When galaxies are far-IR bright ($L_{IR} > 10^{11}$ $L_\odot$), the SFE tends to increase (see equation 3).

assume a $L_{CO\,(J=2-1)}/L_{CO\,(J=1-0)}$ ratio as 0.85, although we reckon this may vary from 0.5 to 1 for different source cases (Carilli & Walter 2013). We expect this systematic variation will affect our result by 0.3 dex at most.

For the 'normal' galaxies at $2 \times 10^9 < L_{IR} < 10^{11}$ $L_\odot$, the SFE′ is roughly constant with scatter of about 0.5 dex, so the SFR and the cold molecular gas mass are roughly proportional to each other (Villanueva et al. 2017). The constant SFE′ indicates that the gas of the normal spiral galaxies is just enough to maintain a long depletion time-scale.

We fit the scaling relation between SFE′ and IR luminosity for all the $L_{IR} > 10^{11}$ $L_\odot$ galaxies from the VALES including our new

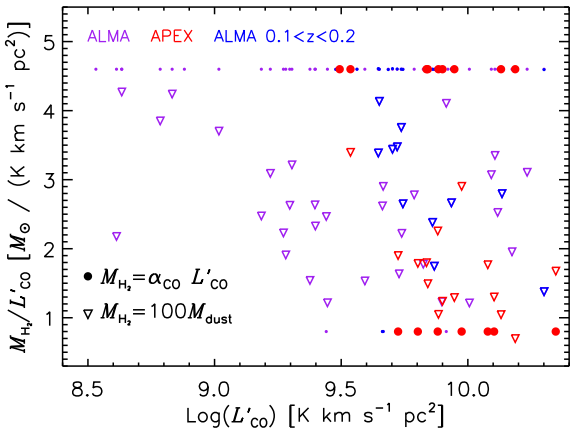

Figure 4. The effective α_{CO} estimate using different methods: the solid circles stand for the method of $M_{H_2} = \alpha_{CO} L'_{CO}$ [$\alpha_{CO} = 0.8\,M_\odot(K\,km\,s^{-1}\,pc^2)^{-1}$ for the mergers and $\alpha_{CO} = 4.6\,M_\odot(K\,km\,s^{-1}\,pc^2)^{-1}$ for the isolated galaxies], the open triangles stand for the method of $M_{H_2} = \delta M_{dust}$, assuming the $\delta = 100$. The ALMA data at $0.1 < z < 0.2$ are represented by blue markers and those outside the range by purple ones.

SEPIA band-5 detections and local ULIRGs taken from (Solomon et al. 1997)

$$\frac{SFE'}{10^{-9}yr^{-1}} = (2.8 \pm 0.9) \times \left(\frac{L_{IR}}{10^{11}\,L_\odot}\right)^{0.71\pm0.01}. \quad (2)$$

The quantities SFE′ and L_{IR} in equation (3) are not independent from each other, nevertheless, this scaling relation can help us to estimate the CO luminosity of low-z LIRGs and ULIRGs.

Previous studies (Magdis et al. 2014; Sargent et al. 2014) have shown that the SFE′ of the spirals and ULIRGs sample in Fig. 3 are consistent with the CO emission surveys at $z < 0.3$, e.g. COLDGASS, EGNoG, and PHIBSS. So we restrict the sample shown in Fig. 3 to spirals and ULIRGs for clarity. The SFE′ in Fig. 3 changes smoothly with the IR luminosity. We do not see a clear separation of SFR modes (Daddi et al. 2010). We note that our LIRG sample bridges the parameter space between the normal SFGs and the local powerful ULIRGs.

4 DISCUSSION

4.1 The origin of the SFE scatter

To understand the true SFE distribution of our sample, we need to tackle the molecular gas content. We use the $M_{H_2} = \alpha_{CO} L'_{CO}$ relation as the primary estimator. To maintain consistency with previous VALES papers in this series, we follow the choice of α_{CO} based on the optical SDSS morphology as in Villanueva et al. (2007): $\alpha = 0.8\,M_\odot(K\,km\,s^{-1}\,pc^2)^{-1}$ for merger systems and $\alpha = 4.6\,M_\odot(K\,km\,s^{-1}\,pc^2)^{-1}$ for isolated disky or bulgy galaxies (Solomon & Vanden Bout 2005; Bolatto et al. 2013).

The H_2 mass can also be estimated from the gas-to-dust ratio. We assume a constant gas-to-dust ratio $\delta = M_{gas}/M_{dust} = 100$ (Magdis et al. 2012), where M_{dust} is derived from the MAGPHYS fits. The typical range of the $M_{dust} \sim 10^{7.5-8.6}\,M_\odot$ and the results are listed in Table 1. The results are illustrated in Fig. 4. Observationally, a typical range of the δ is from about 50 to 150 (Magdis et al. 2012); hence, this can change the M_{H_2}/L'_{CO} from 0.5 to 1.5 times of the current value. As an independent approach of estimating the molecular mass, the gas-to-dust ratio method shows a good agreement with the $\alpha_{CO} L'_{CO}$ estimations (see also Hughes et al. 2017b).

The SFE results are illustrated in Fig. 5. In this figure, we identify two populations of SFGs: one as an extension of the 'main sequence' galaxies with higher SFRs up to $L_{IR} \sim 10^{11.5}\,L_\odot$, the other population has SFE between the 'main sequence' and ULIRGs with a clear trend towards high SFE at higher L_{IR}. The SFE based on the gas-to-dust ratio method suggests a population filling the parameter space between the normal spirals and ULIRGs (Fig. 5). Our observations reveal the existence of a wide range of SFE (specially between $L_{IR} \simeq 10^{11-12}\,L_\odot$), combining both star formation modes: 'disc-like' and 'starburst' features.

Looking at the scatter of the correlation in Fig. 5, we find that the SFE should be anticorrelated with the galaxy gas radius[2]. Fig. 6 shows the ALMA resolved CO radius (R_{CO}) against the SFR/$M_{gas}^{1.4}$, which highlights the importance of the R_{CO} in controlling the SFE. For the more normal SFGs (resolved by ALMA at 3.5 arcsec), we find that the physical sizes of the CO emitting regions tend to be larger for lower SFE, whereas compact CO emitters tend to have higher SFE. For all of the LIRGs observed by APEX (unresolved in CO), we use the SDSS r band Petrosian radius to estimate the $R_{CO} \simeq R_r/1.6$ following Villanueva et al (2017) and show the results in Fig. 6. We find that all of the APEX targets have similar CO radii, which is mainly caused by the narrow redshift range and the limited spatial resolution of SDSS.

For normal SFGs, the main sequence shows SFR $\sim M_*^\beta$, where $\beta \simeq 0.6$ for local galaxies (Brinchmann et al. 2004). The typical gas fractions ($f_g = M_{H_2}/(M_* + M_{H_2})$) of local galaxy samples are of about 10 per cent (Narayanan, Bothwell & Davé 2012b). If the SFR $\propto L_{IR}$, then the combination of these three relations will result in SFE $\propto (1/f_g - 1)L_{IR}^{\frac{\beta-1}{\beta}}$. The β index describes the slope of the SFE and L_{IR} relation, whereas the f_g accounts for the Y-axis intercept (the green lines in Fig. 5).

Finally, considering that APEX measured the total CO flux within a primary beam of ∼35 arcsec at ∼ 200GHz, which is larger than the typical size of a $z \sim 0.1$ galaxy, in the case of merging systems, close counterparts may also contribute to the CO flux. This may be the case, for example, of HATLAS J121005.9+002639, where we see a possible broadening of the CO line emission. This broadening could be due to a close counterpart that is at the same redshift, as seen in Fig. 2. We also note that parameters such as M_* could be affected too. Nevertheless, we estimate that the total stellar mass within the 35 arcsec is no more than ∼2 times larger than the stellar mass of the central galaxy. Thus, the stellar mass will not significantly affect the main trends we find in our data.

4.2 Confronting the bimodality in star formation efficiencies

Previous studies have shown that the SFE in SFGs follow a bimodal behaviour for normal and starburst galaxies (Daddi et al. 2010; Genzel et al. 2010). Based on the existence of the 'main sequence' followed by normal SFGs, Sargent et al. (2014) show that this bimodal SFE can be nicely illustrated by plotting SFE/SFE$_{ms}$ versus sSFR/sSFR$_{ms}$, where SFE/SFE$_{ms}$ is the SFE normalized by the SFE of the main sequence or strongly starbursting galaxies with

[2] The Kennicutt–Schmidt law follows $\Sigma_{SFR} \propto \Sigma_{gas}^{1.4}$. If we make the rough assumption that the SFR $\simeq \Sigma_{SFR} R^2$ and $M_{gas} \simeq \Sigma_{gas} R^2$, then the $\Sigma_{SFR} R^2 \propto \Sigma_{gas}^{1.4} R^{2.8} R^{-0.8}$. So, SFR/$M_{gas}^{1.4} \propto R^{-0.8}$. Since the SFR/$M_{gas}^{1.4}$ is monotonic with SFE, if the Kennicutt–Schmidt law is valid for all the galaxies, galaxies with small gas radii would have higher SFE.

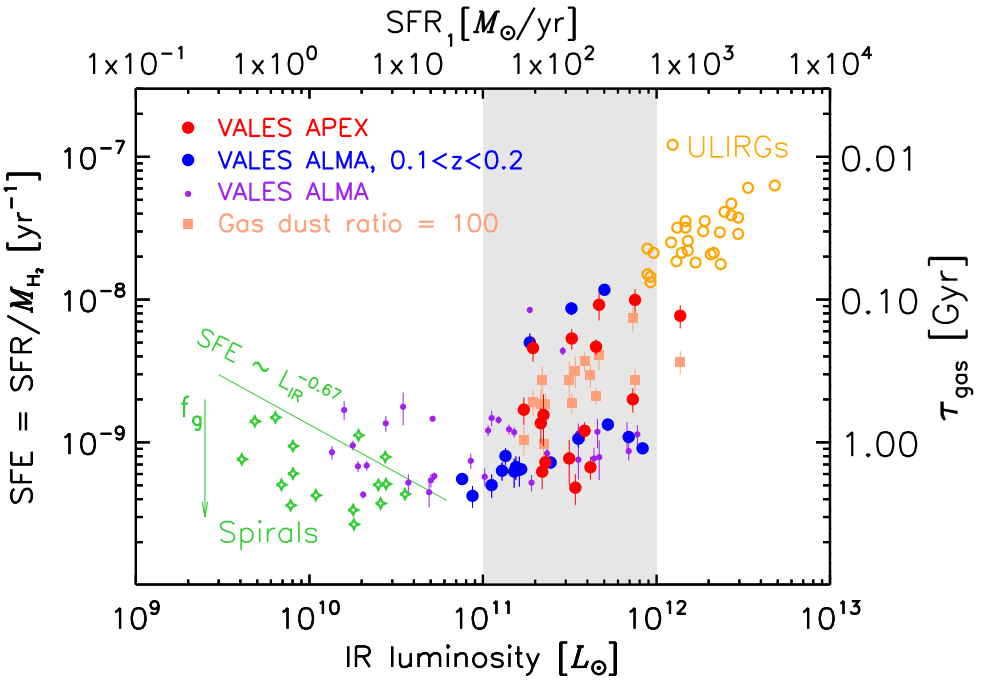

Figure 5. The SFE versus L_{IR} relation. The colour and symbol codes are the same as Fig. 3. We estimate the M_{H_2} with two methods: assuming an α_{CO} that depends on the optical morphology (solid circles) and considering a simple gas-to-dust mass ratio (solid squares). We adopt the $\alpha_{CO} = 4.6\,M_\odot(K\,km\,s^{-1}\,pc^2)^{-1}$ for the isolated galaxies and $\alpha_{CO} = 0.8\,M_\odot(K\,km\,s^{-1}\,pc^2)^{-1}$ for the merging galaxies to derive the M_{H_2} from L'_{CO}, as in previous papers of the VALES series. The *H*-ATLAS data allow deriving the galaxy dust masses, which can be converted into H_2 mass by assuming the gas-to-dust ratio $\delta = M_{gas}/M_{dust} = 100$ (Magdis et al. 2012). Typical values for δ are in the range of 50–150, which can be affect the range of M_{H_2} by 0.3 dex. The SFE of the APEX data nicely bridge the gap between the normal star forming local galaxies and the local ULIRGs. The shaded region corresponds to that where the SFE transitions occurs.

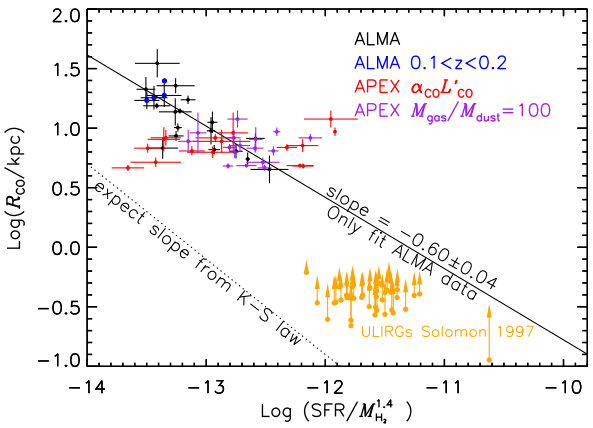

Figure 6. The radius versus the SFR/$M_{gas}^{1.4}$ for all the ALMA resolved galaxies and the APEX targets. The SFR/$M_{gas}^{1.4}$ shows a monotonic relation with SFE. For the ALMA resolved galaxies, the slope of the correlation is about −0.6±0.04. We also show the −0.8 slope as a dashed line, which is expected from the Kennicutt–Schmidt law. We do not have enough resolution for the APEX targets' CO radius (R_{CO}), so we use their SDSS *r* band Petrosian radii/1.6 instead (Villanueva et al. 2017). The orange dots show the lower limits of the radii of ULIRGs sample of the Solomon et al. (1997).

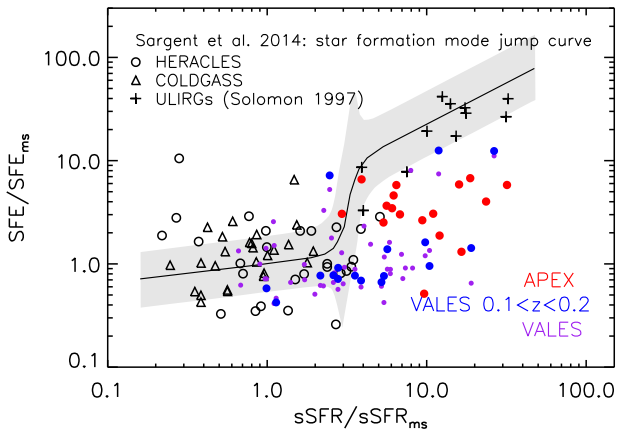

Figure 7. The SFR–SFE relation as shown in fig. 11 in Sargent et al. (2014). We employ the normal galaxies case equation (4) in Sargent et al. (2014) to derive the SFE/SFE$_{ms}$ Here, we only plot the representative samples in Sargent et al. (2014), and we show their result by thick line as well as the uncertainty by the shaded region. The VALES (blue and purple bullets) and APEX (red bullets) samples show a large range along the sSFR/sSFR$_{ms}$ and they are not only consistent with the local normal SFGs at the low sSFR/sSFR$_{ms}$ end but also transition smoothly between the normal SFGs and the ULIRGs.

the same mass. In Fig. 7, we show our VALES (including the new APEX/SEPIA Band-5 detections) sample in comparison with other samples taken from the literature, overplotted over the predictions (solid line) by Sargent et al. (2014). We find that the steep jump in SFE at sSFR/sSFR$_{ms}$ > 3 is not as clean as expected. We highlight that our sample covers a much wider range of sSFRs, with IR luminosities in the LIRGs range in between of those normal (HERACLES and COLDGASS) and local ULIRGs. Indeed, it is evident that Sargent et al. (2014)'s predictions are significantly affected by low number statistics of the most strongly starbursting galaxies (specially at sSFR/sSFR$_{ms}$ > 3). Our study clearly shows that the most 'starbursty' galaxies (see VALES range in Fig. 1) present a wide range of SFEs, i.e. not all galaxies with high sSFR are passing through a dominant starburst phase. As shown in Fig. 3, there is

a smooth transition of SFEs as a function of IR luminosities, in contradiction with a bimodal behaviour.

Our evidence is also supported by a recent study by Lu et al. (2017), using local LIRGs, which shows a similarly smooth transition in SFEs as analysed by the [CI]370 μm/CO(7–6) and C(60 μm/100 μm) ratios (fig. 17, panel c in their paper). Here, we will consider the CO(7–6) as a proxy for the SFR and [CI]370 μm as a proxy for the M_{H_2} (Jiao et al. 2017). Lu et al. (2017) suggest that the change in effective SFE could be correlated to the far-IR colour, i.e. the dust temperature. Another study by Michiyama et al. (2016) on a sample of 26 nearby merging galaxies with ASTE CO (3-2) observation also confirmed the smooth transition of SFE on the local galaxies. On the other hand, a smooth transition of the SFE is also found by the recent study by Lee et al. (2017), using a sample of 20 intermediate redshift ($0.25 < z < 0.65$) LIRGs in the Cosmological Evolution Survey (COSMOS). We conclude that our findings are consistent with previous studies of LIRGs at low and intermediate redshifts.

We have identified different parameters responsible for the observed scatter of the SFE in SFGs, nevertheless the only parameter that most probably causes the appearance of a bimodal behaviour comes from the bimodal assumption of the α_{CO} conversion factor. It is well known that α_{CO} is dependent on the physical properties of the ISM (e.g. metallicity, density, temperature; Solomon & Vanden Bout 2005), so that making a global assumption for a single α_{CO} value over the whole galaxy can be significantly affected by complex systematical uncertainties (e.g. Sandstrom et al. 2013).

5 CONCLUSION

Our new APEX/SEPIA Band-5 observations double the number of sources with CO detections in the ALMA-based VALES sample at $0.1 < z < 0.2$, specially covering the parameter space at higher sSFR. In this work, we concentrate in an investigation of the global SFE of CO-detected galaxies, including previous low-z surveys taken from the literature. To avoid the uncertainties on the α_{CO} conversion factor, we explore the correlation between the SFR/L'_{CO} ratio and the IR luminosity. We find that this ratio remains relatively constant up to $L_{IR} \sim 10^{11}\,L_{\odot}$ (a scatter of ~ 0.5 dex), although above this value, there is a clear increment in the effective SFE. Benefited by the large sSFR/$sSFR_{ms}$ of our VALES and APEX sample, we find a smooth transition of the SFE instead of a steep jump from the normal SFGs to the ULIRGs. The smooth increment as a function of far-IR luminosity (specially between $10^{11-12}\,L_{\odot}$) is consistent with the previous LIRGs study (Lee et al. 2017; Lu et al. 2017). This suggests that the dominating star formation mechanism (starburst or disc-like) smoothly changes between powerful ULIRGs and normal galaxies. We conclude that the main parameters controlling the scatter of the global SFE versus LIR correlation are the assumed α_{CO} conversion factor, the gas fraction, and the physical size of the galaxies.

ACKNOWLEDGEMENTS

This paper benefited from a number of thoughtful comments made by the anonymous referee. This work was support from the Chinese Academy of Sciences (CAS) through the CASSACA Postdoc Grant and the Visiting Scholarship Grant administered by the CAS South America Center for Astronomy (CASSACA), NAOC. EI and TMH acknowledge the CONICYT/ALMA funding Program in Astronomy/PCI Project N°: 31140020. EI acknowledges partial support from FONDECYT through grant N° 1171710. TMH acknowledges the support from the Chinese Academy of Sciences (CAS) and the National Commission for Scientific and Technological Research of Chile (CONICYT) through a CAS-CONICYT Joint Postdoctoral Fellowship administered by the CAS South America Center for Astronomy (CASSACA) in Santiago, Chile. RL acknowledges the support from Comité Mixto ESO-GOBIERNO DE CHILE and GEMINI-CONICYT FUND 32130024. AMA acknowledges the support provided by CONICYT (Chile) through FONDECYT postdoctoral research grant No 3160776. GO acknowledges the support provided by CONICYT (Chile) through FONDECYT postdoctoral research grant no 3170942. CKX acknowledges the support of NSFC-11643003. NL acknowledges the support by the NSFC grant #11673028 and by the National Key R&D Program of China grant #2017YFA0402704. YQX acknowledges the support of NSFC-11473026 and 11421303. This publication is based on data acquired with the Atacama Pathfinder Experiment (APEX). APEX is a collaboration between the Max-Planck-Institut fur Radioastronomie, the European Southern Observatory, and the Onsala Space Observatory. This paper makes use of the following ALMA data: ADS/JAO.ALMA 2012.1.01080.S and ADS/JAO.ALMA 2013.1.00530.S. ALMA is a partnership of ESO (representing its member states), NSF (USA), and NINS (Japan), together with NRC (Canada), NSC and ASIAA (Taiwan), and KASI (Republic of Korea), in cooperation with the Republic of Chile. The Joint ALMA Observatory is operated by ESO, AUI/NRAO, and NAOJ.

REFERENCES

Armus L. et al., 2009, PASP, 121, 559
Bauermeister A. et al., 2013, ApJ, 768, 132
Belitsky V. et al., 2017, preprint (arXiv:1712.07396)
Billade B. et al., 2012, IEEE Trans. Terahertz Sci. Technol., 2, 208
Bolatto A. D., Wolfire M., Leroy A. K., 2013, ARA&A, 51, 207
Brinchmann J., Charlot S., White S. D. M., Tremonti C., Kauffmann G., Heckman T., Brinkmann J., 2004, MNRAS, 351, 1151
Carilli C. L., Walter F., 2013, ARA&A, 51, 105
Chabrier G., 2003, ApJ, 586, L133
Combes F., 2016, Proc. IAU Symp., 315, From Interstellar Clouds to Star-Forming Galaxies: Universal Processes? Kluwer, Dordrecht, p. 240C
Combes F., García-Burillo S., Braine J., Schinnerer E., Walter F., Colina L., 2011, A&A, 528, A124
Combes F., García-Burillo S., Braine J., Schinnerer E., Walter F., Colina L., 2013, A&A, 550, A41
Costagliola F., Aalto S., Sakamoto K, Martín S., Beswick R., Muller S., Kl'ockner H.-R., 2013, A&A, 556, 66
da Cunha E., Charlot S., Elbaz D., 2008, MNRAS, 388, 1595D
Daddi E. et al., 2010, ApJ, 714, L118
Downes D., Solomon P. M., 1998, ApJ, 507, 615
Driver S. P. et al., 2016, MNRAS, 455, 3911
Eales S. et al., 2010, PASP, 122, 499C
Elbaz D. et al., 2011, A&A, 533, 119
Genzel R. et al., 2010, MNRAS, 407, 2091
Genzel R. et al., 2015, ApJ, 800, 20
Hughes T. M. et al., 2017a, A&A, 602, 49
Hughes T. M. et al., 2017b, MNRAS, 468, L103
Jiao Q., Zhao Y., Zhu M., Lu N., Gao Y., Zhang Z.-Y., 2017, ApJ, 840, L18
Lee N. et al., 2017, MNRAS, 471, 2124
Leroy A. K. et al., 2009, AJ, 137, 4670
Lonsdale C. J., Farrah D., Smith H. E., 2006, Astrophysics Update 2. Springer Praxis, Chichester, p. 285
Lu N. et al., 2017, ApJS, 230, 1
Magdis G. E. et al., 2012, ApJ, 760, 6
Magdis G. E. et al., 2014, ApJ, 796, 63M

Michiyama T. et al., 2016, PASJ, 68, 96
Narayanan D., Krumholz M., Ostriker E. C., Hernquist L., 2011, MNRAS, 418, 664
Narayanan D., Krumholz M. R., Ostriker E. C., Hernquist L., 2012a, MNRAS, 421, 3127N
Narayanan D., Bothwell M., Davé R., 2012b, MNRAS, 426, 1178N
Papadopoulos P. P., Thi W.-F., 2013, in Astrophysics and Space Science Library, Vol. 34, Cosmic Rays in Star-Forming Environments. Springer-Verlag, Berlin, p. 41P
Papadopoulos P. P., van der Werf P. P., Xilouris E. M., Isaak K. G., Gao Y., Mühle S., 2012a, MNRAS, 426, 2601
Papadopoulos P. P., van der Werf P., Xilouris E., Isaak K. G., Gao Y., 2012b, ApJ, 751, 10P
Saintonge A. et al., 2011, MNRAS, 415, 32
Sandstrom K. M. et al., 2013, ApJ, 777, 5S
Sargent M. T. et al., 2014, ApJ, 793, 19
Schawinski K. et al., 2014, MNRAS, 440, 889S
Schreiber C. et al., 2015, A&A, 575, 74
Sliwa K. et al., 2013, ApJ, 777, 126
Solomon P. M., Vanden Bout P. A., 2005, ARA&A, 43, 677
Solomon P. M., Downes D., Radford S. J. E., Barrett J. W., 1997, ApJ, 478, 144
Speagle J. S., Steinhardt C. L., Capak P. L., Silverman J. D., 2014, ApJS, 214, 15
Tunnard R., Greve T. R., Garcia-Burillo S., Graciá Carpio J., Fuente A., Tacconi L., Neri R., Usero A., 2015, ApJ, 815, 114
Valiante E. et al., 2016, MNRAS, 462, 3146
Villanueva V. et al., 2017, MNRAS, 470, 3775
Whitaker K. E., van Dokkum P. G., Brammer G., Franx M., 2012, ApJ, 754, 29
Xu C. K. et al., 2014, 787, 48
Xu C. K. et al., 2015, ApJ, 799, 11
Yao L., Seaquist E. R., Kuno N., Dunne L., 2003, ApJ, 588, 771

This paper has been typeset from a TEX/LATEX file prepared by the author.